


















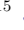






High Tide or Rip-Tide on the Cosmic Shoreline? A Water-Rich Atmosphere or Stellar Contamination for the Warm Super-Earth GJ 486b from JWST Observations

SARAH E. MORAN ¹, KEVIN B. STEVENSON ², DAVID K. SING ^{3,4}, RYAN J. MACDONALD ^{5,6}, JAMES KIRK ⁷,
JACOB LUSTIG-YAEGER ², SARAH PEACOCK ^{8,9}, L. C. MAYORGA ², KATHERINE A. BENNETT ³,
MERCEDES LÓPEZ-MORALES ¹⁰, E. M. MAY ², ZAFAR RUSTAMKULOV ³, JEFF A. VALENTI ¹¹,
JÉA I. ADAMS REDAI ¹⁰, MUNAZZA K. ALAM ¹², NATASHA E. BATALHA ¹³, GUANGWEI FU ⁴,
JUNELLIE GONZALEZ-QUILES ³, ALICIA N. HIGHLAND ⁵, ETHAN KRUSE ^{9,14,15}, JOSHUA D. LOTHINGER ¹⁶,
KEVIN N. ORTIZ CEBALLOS ¹⁰, KRISTIN S. SOTZEN ^{2,3} AND HANNAH R. WAKEFORD ¹⁷

¹*Department of Planetary Sciences and Lunar and Planetary Laboratory, University of Arizona, Tucson, AZ, USA*

²*Johns Hopkins APL, Laurel, MD, 20723, USA*

³*Department of Earth & Planetary Sciences, Johns Hopkins University, Baltimore, MD, USA*

⁴*Department of Physics & Astronomy, Johns Hopkins University, Baltimore, MD, USA*

⁵*Department of Astronomy, University of Michigan, 1085 S. University Ave., Ann Arbor, MI 48109, USA*

⁶*NHFP Sagan Fellow*

⁷*Department of Physics, Imperial College London, Prince Consort Road, London, SW7 2AZ, UK*

⁸*University of Maryland, Baltimore County, MD 21250, USA*

⁹*NASA Goddard Space Flight Center, Greenbelt, MD 20771, USA*

¹⁰*Center for Astrophysics | Harvard & Smithsonian, 60 Garden St, Cambridge, MA 02138, USA*

¹¹*Space Telescope Science Institute, Baltimore, MD 21218, USA*

¹²*Carnegie Earth & Planets Laboratory, Washington, DC, 20015, USA*

¹³*NASA Ames Research Center, Moffett Field, CA, USA*

¹⁴*Department of Astronomy, University of Maryland, College Park, MD 20742.*

¹⁵*Center for Research and Exploration in Space Science and Technology, NASA/GSFC, Greenbelt, MD 20771*

¹⁶*Department of Physics, Utah Valley University, Orem, UT, 84058 USA*

¹⁷*School of Physics, HH Wills Physics Laboratory, University of Bristol, Bristol, UK*

Submitted to ApJL

ABSTRACT

Planets orbiting M-dwarf stars are prime targets in the search for rocky exoplanet atmospheres. The small size of M dwarfs renders their planets exceptional targets for transmission spectroscopy, facilitating atmospheric characterization. However, it remains unknown whether their host stars' highly variable extreme-UV radiation environments allow atmospheres to persist. With *JWST*, we have begun to determine whether or not the most favorable rocky worlds orbiting M dwarfs have detectable atmospheres. Here, we present a 2.8–5.2 μm *JWST* NIRSpec/G395H transmission spectrum of the warm (700 K, 40.3 \times Earth's insolation) super-Earth GJ 486b (1.3 R_{\oplus} and 3.0 M_{\oplus}). The measured spectrum from our two transits of GJ 486b deviates from a flat line at 2.2 – 3.3 σ , based on three independent reductions. Through a combination of forward and retrieval models, we determine that GJ 486b either has a water-rich atmosphere (with the most stringent constraint on the retrieved water abundance of $\text{H}_2\text{O} > 10\%$ to 2 σ) or the transmission spectrum is contaminated by water present in cool unocculted starspots. We also find that the measured stellar spectrum is best fit by a stellar model with cool starspots and hot faculae. While both retrieval scenarios provide equal quality fits ($\chi^2_{\nu} = 1.0$) to our NIRSpec/G395H observations, shorter wavelength observations can break this degeneracy and reveal if GJ 486b sustains a water-rich atmosphere.

Keywords: JWST, Terrestrial Exoplanet Atmospheres, Transmission Spectroscopy

1. INTRODUCTION

Understanding the stability and longevity of atmospheres on rocky planets orbiting M dwarfs is paramount for understanding which, if any, of these planets may ultimately support life. However, given the high activity of most M-dwarf stars (e.g., [Peacock et al. 2019](#)), their planets are subject to extreme-UV radiation regimes that may remove any significant atmosphere through escape processes (e.g., [Airapetian et al. 2020](#); [Kasting & Pollack 1983](#); [Zahnle & Catling 2017](#); [Airapetian et al. 2017](#)). This high activity also persists over much longer timescales given the long lifetimes of M dwarfs compared to larger stars (e.g., [Lloyd et al. 2021](#)). M dwarfs also have the potential to impart spurious features into the transmission spectrum from inhomogeneities in the stellar photosphere, a phenomenon called the “Transit Light Source effect” (TLS) ([Rackham et al. 2018](#)), also known as stellar contamination ([Apai et al. 2018](#); [Barclay et al. 2021](#); [Garcia et al. 2022](#); [Barclay et al. 2023](#)).

Rocky worlds ($\leq 1.4R_{\oplus}$) are not predicted to retain hydrogen/helium-dominated atmospheres ([Rogers 2015](#); [Rogers et al. 2021](#)). This has been confirmed by observations of terrestrial planets, including the TRAPPIST-1 planets ([de Wit et al. 2016, 2018](#); [Wakeford et al. 2019](#); [Garcia et al. 2022](#); [Gressier et al. 2022](#)), GJ 1132b ([Diamond-Lowe et al. 2018](#); [Mugnai et al. 2021](#); [Libby-Roberts et al. 2022](#)), the L98-59 system ([Damiano et al. 2022](#); [Zhou et al. 2023](#)), LTT 1445Ab ([Diamond-Lowe et al. 2022](#)) and LHS 3488b ([Kreidberg et al. 2019](#); [Diamond-Lowe et al. 2020](#)). However, many of these observations do not preclude higher mean molecular weight secondary atmospheres for these small planets ([Moran et al. 2018](#); [Damiano et al. 2022](#)).

As part of the Cycle 1 *JWST* General Observer (GO) Program 1981 (PIs: K. Stevenson & J. Lustig-Yaeger), we are searching for atmospheric signatures on rocky planets around M dwarfs. Our program focuses reconnaissance on carbon dioxide (CO_2) and methane (CH_4), believed to produce the strongest signals in terrestrial atmospheres ([Kaltenegger & Traub 2009](#); [Lustig-Yaeger et al. 2019](#)). Both have strong bands between 3 and 5 μm , which can be probed by *JWST*. Secondary atmospheric CO_2 is also potentially common across a range of terrestrial planetary conditions via outgassing ([Lincowski et al. 2018](#)), as seen on Venus, Earth, and Mars. Using *JWST*, Program 1981 has already enabled a strong constraint on Earth-sized exoplanet LHS 475b, ruling out Earth-like, hydrogen/helium, wa-

ter, or methane-dominated clear atmospheres ([Lustig-Yaeger & Fu et al. 2023](#)).

Our ultimate aim is to trace the proposed *cosmic shoreline*, defined by [Zahnle & Catling \(2017\)](#). The cosmic shoreline describes the relationship between a planet’s escape velocity (v_{esc}) and insolation (I). This “shoreline” divides rocky bodies with atmospheres from those without and is shaped by various processes that cause atmospheric loss. In the solar system, this relationship follows $I \propto v_{\text{esc}}^4$, suggesting that atmospheric escape mechanisms are dominated by thermal processes ([Zahnle & Catling 2017](#)). Both thermal processes, such as Jeans escape and hydrodynamic escape, and non-thermal processes, encompassing photochemical escape and ion escape, cause composition-dependent atmospheric loss. These escape processes can be enhanced in planets around active stars through UV flaring or stellar winds. Thus, to understand any putative cosmic shoreline in the solar system or beyond, it is important to determine not only how planet size, mass, and atmospheric composition affect a planet’s ability to retain an atmosphere, but also the effect of the host star’s activity. These varying factors can reveal the mechanisms dominating atmospheric escape on a given world (e.g., [Wordsworth & Kreidberg 2022](#); [McIntyre et al. 2023](#)).

Here we present the results of our JWST-GO-1981 program observations for GJ 486b, a $1.3 R_{\oplus}$ and $3.0 M_{\oplus}$ planet ([Caballero et al. 2022](#)), with a zero Bond albedo equilibrium temperature of 700 K. GJ 486b has one of the highest transmission spectroscopy metrics ([Kemp-ton et al. 2018](#)) of any known terrestrial exoplanet ([Trifonov et al. 2021](#)), making it a favorable target for study. The measured mass and radius indicate that GJ 486b is likely composed of a small metallic core, a deep silicate mantle, and a thin volatile upper layer ([Caballero et al. 2022](#)), which could be resistant to escape given the quiescent M3.5 V host star ($0.339 R_{\odot}$, $T_{\text{eff}} = 3291 \text{ K}$; [Caballero et al. 2022](#)). Recent high-resolution observations of GJ 486b show that the planet does not possess a clear $1\times$ solar atmosphere dominated by hydrogen/helium to high confidence ($\geq 5\sigma$). These observations also suggest that a clear, pure water atmosphere could be ruled out to low significance ($\leq 3\sigma$) ([Ridden-Harper et al. 2022](#)). We contextualize these observations in light of our own findings in Section 5.

2. JWST OBSERVATIONS OF GJ 486b

We observed two transits of GJ 486b using the Near InfraRed Spectrograph (NIRSpec; [Jakobsen et al. 2022](#);

Birkmann et al. 2022) G395H instrument mode, covering wavelengths $2.87 - 5.14 \mu\text{m}$ at an average native spectral resolution $\mathcal{R} \sim 2700$. The G395H grating is split over two detectors, NRS1 and NRS2, with a gap from 3.72 to $3.82 \mu\text{m}$. The first transit observation commenced on 25 December 2022 at 11:38 UTC and the second on 29 December 2022 at 21:15 UTC. Each observation lasted 3.53 hours, which covered the 1.01 hour transit duration and the required baseline. Both observations used the NIRSpec Bright Object Time Series (BOTS) mode with the NRSRAPID readout pattern, S1600A1 slit, and the SUB2048 subarray. For this bright target ($K_{\text{mag}} = 6.4$), we used 3 groups per integration and obtained 3507 integrations per exposure.

3. NIRSPEC G395H DATA REDUCTION

We reduced the data using three separate pipelines: *Eureka!* (Bell et al. 2022), *FIREFLY* (Rustamkulov et al. 2022, 2023), and *Tiberius* (Kirk et al. 2018, 2019, 2021). Each pipeline analysis is described below. Appendix A contains the updated system parameters obtained from each reduction. The three reductions showed a consistent offset in the measured transit depth for the Transit 1, NRS2 detector relative to the other three white light curve depths. We rule out astrophysical effects for this discrepancy and corrected it in each reduction as described in Appendix A.1.

3.1. *Eureka!*

We use a modified version of the *jwst* Stage 1 pipeline, starting from the *_uncal.fits* files. We perform group-level background subtraction before determining the flux per integration. For each group, we exclude the region within 9 pixels of the trace before computing and subtracting a median background value per pixel column. We process the *_rateints.fits* files through the regular *jwst* Stage 2 pipeline, skipping the flat fielding and absolute photometric calibration steps when our goal is to derive the planet’s spectrum at later stages. Conversely, we include these steps when our goal is to compute the flux-calibrated stellar spectrum (see Section 4.4). Stage 3 of *Eureka!* converts the time-series of 2D integrations into 1D spectra using optimal spectral extraction (Horne 1986) and an aperture within 5 pixels of the trace. We flag bad pixels at numerous points within this stage using thresholds optimized to minimize scatter in the white light curves.

For the NRS1 detector, we extract the flux from $2.777 - 3.717 \mu\text{m}$ and split the light into 47 spectroscopic light curves, each 20 nm ($0.02 \mu\text{m}$) in width. For the NRS2 detector, we adopt the same resolution in extracting 67 spectroscopic light curves spanning $3.825 - 5.165 \mu\text{m}$.

For each detector, we manually mask 9 pixel columns that exhibit significant scatter in their individual light curves. Doing so improves the quality of the spectroscopic light curves and yields more consistent transit depths.

With two NIRSpec detectors and two transit observations, we fit four white light curves and their systematics (see Figure 1). We determine the system parameters using *batman* (Kreidberg 2015) and fix the quadratic limb-darkening coefficients to those provided by ExoTiC-LD (Grant & Wakeford 2022), assuming the stellar parameters given by Trifonov et al. (2021) and the MPS-ATLAS set 1 models (Kostogryz et al. 2023). For the NRS1 detector, we find that a quadratic trend in time provides the best fit. For the NRS2 detector, a linear trend suffices to remove systematics. Table 1 lists our best-fit system parameters.

Fig. Set 1. Spectroscopic and White Light Curves of GJ 486b

When fitting the spectroscopic light curves (see Figure 1), we fix the planet’s transit midpoint, inclination, and semi-major axis to the weighted mean values in Table 1. We fix the quadratic limb-darkening parameters to the values provided by ExoTiC-LD for each spectroscopic channel. For the NRS1 detector, we also fix the quadratic term in our time-dependent systematic model to that of the best-fit white light curve value (Transit 1: $c_2 = 0.0335$, Transit 2: $c_2 = 0.0248$). For all spectroscopic light curves, we fit for the zeroth and first-order terms (c_0 and c_1) of our polynomial. Light curves from the NRS2 detector only require a linear model in time. Including the term that rescales the uncertainties, each spectroscopic light curve has four free parameters, of which only the planet-to-star radius ratio is a physical parameter.

For each light curve, we first perform a least-squares minimization using the Powell method (Powell 1964) and then initialize our MCMC routine using our best-fit values. We estimate the parameter uncertainties using *emcee* (Foreman-Mackey et al. 2013) and, at each iteration, we increase the uncertainties by an average factor of ~ 1.5 to achieve a reduced $\chi^2 = 1$. All of our posteriors are Gaussian distributed and there are no parameter degeneracies.

3.2. *FIREFLY*

We run the *jwst* pipeline through Stages 1 and 2 using the *_uncal.fits* files. We utilize group-level 1/f subtraction and apply a scaled superbias to account for the vertical offset seen in NRS2 Transit 1. (See Section A.1.) We correct for cosmic rays and bad and hot pixels in the Stage 2 output *_rateints.fits* files and apply a second

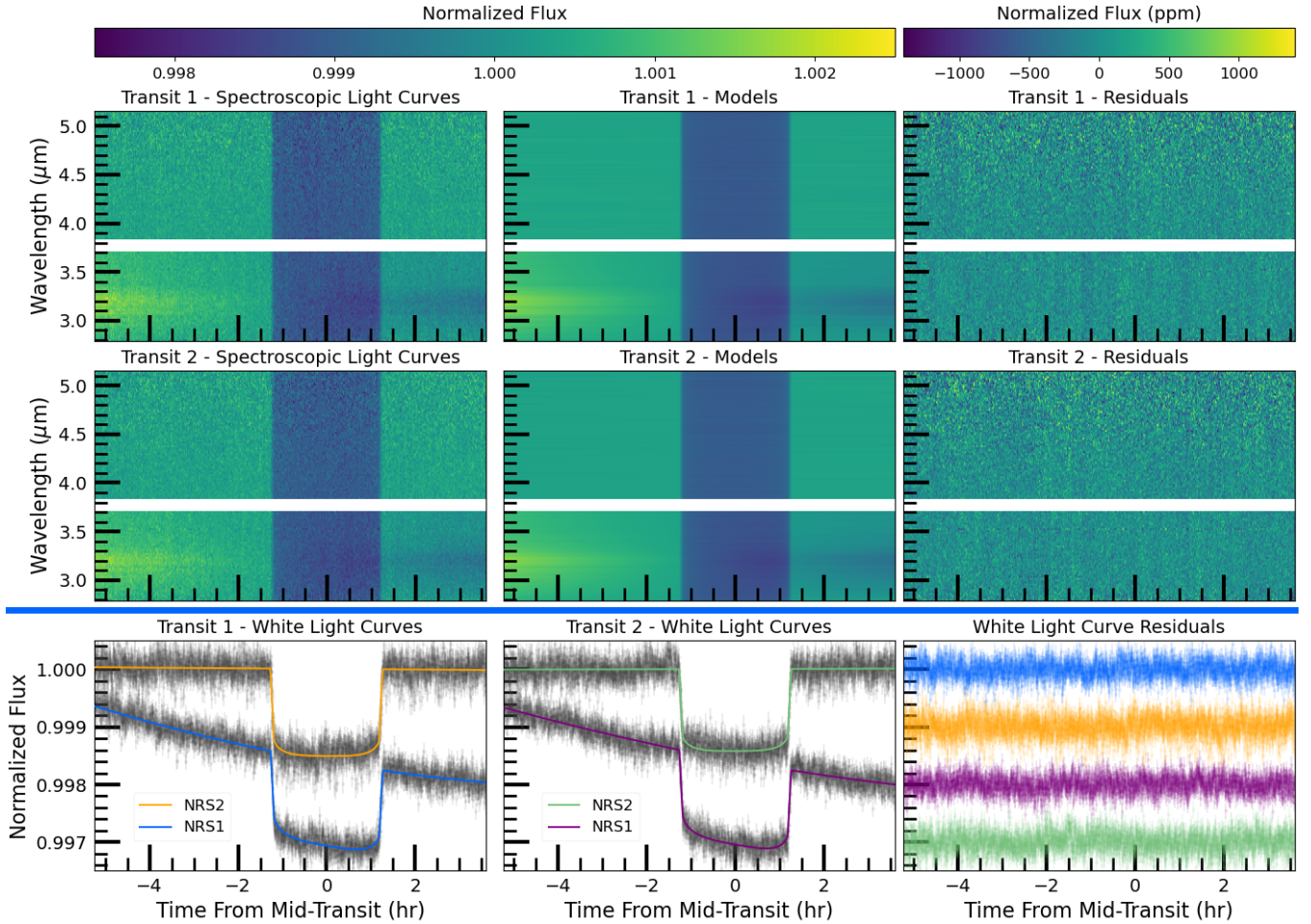


Figure 1. Eureka! spectroscopic and white light curves from two transits of GJ 486b. The top two rows contain the spectroscopic light curves (left), our best-fit models (center), and subsequent residuals (right) for each transit. Most evident in the data are wavelength-dependent ramps near 3.2 μm that we readily remove. The bottom row depicts the white light curves from each detector (NRS1 and NRS2) after removing their systematic trends. Correlated noise is evident in the residuals and is likely due to thermal cycling (Rigby et al. 2022). The standard deviation of the normalized residuals is 140 ppm for NRS1 and 165 ppm for NRS2. The complete figure set (3 images, one for each reduction) is available in the online journal.

1/f correction at the integration level by masking the spectral trace and then calculating the median of the background pixels in each column. This value is then subtracted from the cleaned 2D image.

We next cross-correlate each 2D image with the median aligned image to determine the x- and y-shifts of the spectral trace, which are used to align all 2D images. A Gaussian profile is then cross-correlated to each column in the y-direction and a fourth-order polynomial is fit in the x-direction to determine the spectral trace, which is used to extract the spectra.

The white light curves for Transits 1 and 2 are fit from the extracted spectra by summing the spectra in the wavelength direction over a detector. We fit a/R_\star , limb darkening parameters, and the impact parameter b using the weighted mean from both transits and both detectors. We then fix a/R_\star , b , and the period, and fit

for R_P/R_\star , T_0 , and limb darkening in the white light curve. A low-order polynomial in time (third-order in NRS1 and up to fourth-order for NRS2) was used to model the baseline, with additional detrending parameters of the x- and y-shifts and superbias scale factor. We then fix the system parameters (presented in Table 2) and limb-darkening coefficients in each wavelength column to fit the spectroscopic light curves.

3.3. Tiberius

With Tiberius we started by running STScI's `jwst` stage 0 pipeline on the `uncal.fits` files from the `group_scale` step through `gain_scale` step. We set `--odd_even_columns = True` at the `ref_pix` step and ran our own 1/f correction step at the group level prior to running `ramp_fit`, which removes the median background flux for every column of every group's spec-

tral image. We define the background as a 14-pixel-wide region that avoided 18 pixels centered on the curved trace, and mask bad pixels using our own custom bad pixel map. We subsequently ran `assign_wcs` and `extract_2d` to obtain the wavelength solution and proceeded to run Tiberius’s spectral extraction on the `gainscalestep.fits` files.

First we oversampled each pixel by a factor of 10 using a linear interpolation. This allows us to measure the stellar flux at the sub-pixel level, which reduces noise in the light curves (The JWST Transiting Exoplanet Community Early Release Science Team et al. 2022). We used a fourth order polynomial to trace the NRS1 detector stellar spectrum and a sixth order polynomial for NRS2. We performed standard aperture photometry at every pixel column, with a 4-pixel-wide aperture. We performed an additional background subtraction step at this stage by calculating the background in 14 pixels on either side of the trace, excluding 7 pixels on each side. For NRS1 we fit these background pixels with a linear polynomial while for NRS2 we used a median since our defined background regions were mostly above the stellar trace.

We remove cosmic rays and residual bad pixels manually and then correct for small shifts in the stellar spectra along the dispersion direction by cross-correlating all spectra in the time-series with the first, resampling each spectrum onto a common pixel grid. Finally, we created a white light curve between 2.75–3.72 μm for NRS1 and 3.83–5.15 μm for NRS2. Our spectroscopic light curves were created at 1 pixel resolution over the same wavelength range.

We fit the four white light curves (2 transits \times 2 detectors) with `batman` (Kreidberg et al. 2015), leaving a/R_* , R_P/R_* , the orbital inclination (i), and the time of mid-transit (T_0) as free parameters, and fixing the period to the value from Trifonov et al. (2021). For our white and spectroscopic light curves, we assumed quadratic limb darkening with coefficients fixed to values from 3D stellar atmosphere models (Magic et al. 2015) using ExoTiC-LD (Grant & Wakeford 2022). We adopted $T_{\text{eff}} = 3340 \text{ K}$, $[\text{Fe}/\text{H}] = 0.070$ and $\log g_* = 4.9155$ (Trifonov et al. 2021). For our systematics model we used a combination of polynomials: quadratic-in-time, linear-in-x-position, and linear-in-y-position, resulting in 9 free parameters: 4 transit model parameters and 5 systematics model parameters.

To determine the best fitting values and uncertainties, we used `emcee` (Foreman-Mackey et al. 2013) with 90 walkers for two runs of 20,000 steps. After the first run we inflated our photometric uncertainties to give a reduced $\chi^2 = 1$ for our best-fitting model before the sec-

ond run. Table 3 summarizes the results of our white light curve fits. For our spectroscopic light curve fits, we fixed a/R_* , i and T_0 to the weighted mean values from our 4 white light curve fits and only fitted for R_P/R_* and the 5 parameters defining our systematics model. Here we used a Levenberg-Marquadt sampler for computational speed as we had to fit 6876 spectroscopic light curves.

4. INTERPRETATION OF GJ 486b’S TRANSMISSION SPECTRUM

The three data reductions produce consistent spectra with a slight slope on the blue end ($\leq 3.7 \mu\text{m}$) but are otherwise featureless. Here, we first quantify the significance of this slope in GJ 486b’s spectrum. We then proceed to offer physical explanations of the spectrum through forward modeling and retrieval analyses.

4.1. A Non-Flat Spectrum

We performed a flat line hypothesis rejection test to determine the statistical significance of the slope in the transmission spectrum. We fitted the spectrum from each pipeline using two models: a flat featureless model that uses one free parameter for the transit depth, and a Gaussian spectral feature model with four free parameters: the flat transit depth and the central wavelength, amplitude, and width of a Gaussian feature added to the baseline featureless spectrum. We fitted both models to each dataset using the `dynesty` nested sampling code for Bayesian inference (Speagle 2020) and then used the Bayesian evidence to calculate the Bayes factor of each model (e.g., Trotta 2008, 2017). We then converted the Bayes factors to more classical “sigma” detection significances using the relationship detailed by Benneke & Seager (2013).

Figure 2 demonstrates that each spectrum separately favors the Gaussian model and rejects a featureless spectrum. The strength of the signal detection is 3.20σ for Eureka!, 2.24σ for FIREFLY, and 3.29σ for Tiberius. The FIREFLY detection significance is lower due to slightly larger uncertainties associated with that reduction, which stem from FIREFLY’s choice of spectroscopic binning to produce similar transit depth errors across the full wavelength range and wavelength-dependent baseline functions. Nevertheless, the same shape is seen in the spectra from the three pipelines. Thus, the flat line hypothesis is rejected by all three analyses with varying confidence. Each individual reduction hypothesis rejection test is available in the online journal.

Fig. Set 2. Data and Gaussian Fitting Tests

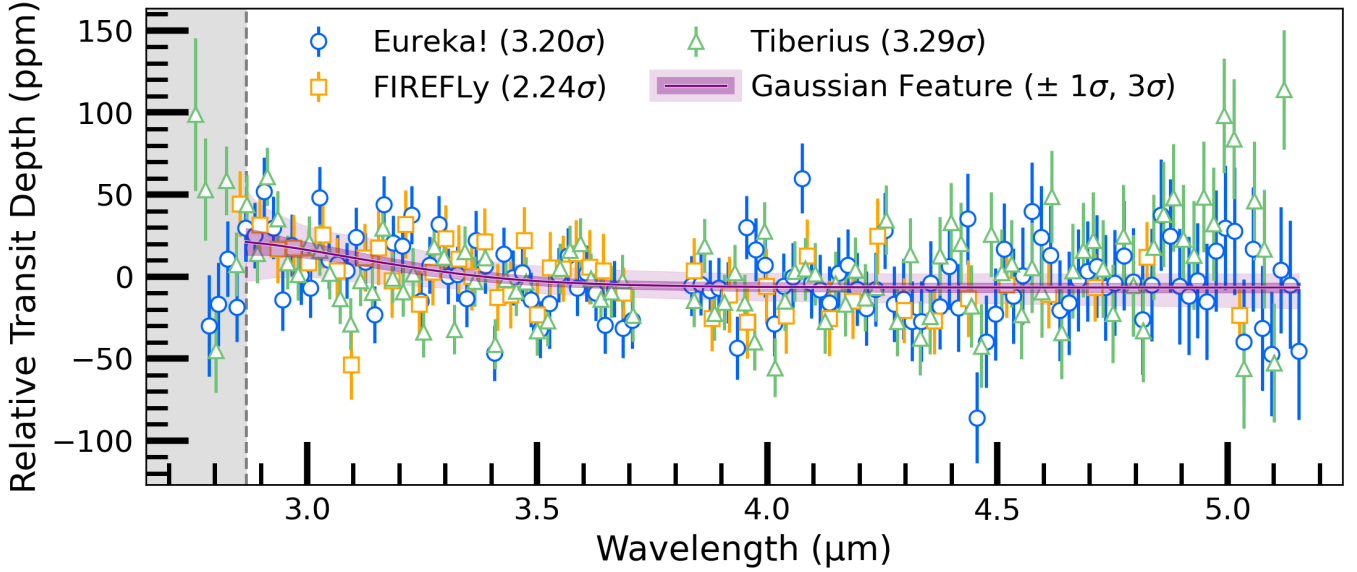


Figure 2. Relative transmission spectra of the three data reductions (**Eureka!**: blue circles, **FIREFLY**: orange squares, **Tiberius**: green triangles). The median fit to the **Eureka!** dataset using an agnostic Gaussian model is shown in purple bounded by 1σ and 3σ Bayesian credibility envelopes. The legend displays the statistical significance with which each reduction rules out a flat line in favor of the Gaussian model. Analyses of all three reductions reveal an uptick at the blue end of the wavelength range. Instrument throughput deteriorates in the grey shaded region and the measured transit depths become unreliable; thus we exclude points within this region from our hypothesis rejection tests.

4.2. Forward Modeling Tentatively Supports an Atmosphere with Water Vapor

We ran a suite of forward models using the stellar and planet parameters from Caballero et al. (2022) to compare to each transmission spectrum. We also generated forward models using an updated stellar $\log(g) = 4.91 \pm 0.02$, obtained from our updated a/R_s constraints (See Appendix A) (Seager & Mallén-Ornelas 2003; Sandford & Kipping 2017), finding consistent results.

We focus on higher mean molecular weight scenarios to explain the transmission spectrum. For completeness, however, we simulate a $1000\times$ solar metallicity atmosphere with a parameterized pressure-temperature profile in thermochemical equilibrium with CHIMERA (Line & Yung 2013; Line et al. 2014) as in our previous work (Lustig-Yaeger et al. 2023). We include the species H_2O , CH_4 , CO , CO_2 , NH_3 , HCN , H_2S , H_2 , and He . The CHIMERA thermochemical equilibrium abundances result in a model spectrum that is primarily shaped by methane, carbon dioxide, and water. After generating the temperature-pressure profile and atmospheric abundances with CHIMERA, we use the radiative transfer suite of PICASO (Batalha et al. 2019), with opacities resampled to $R = 10,000$ from Batalha et al. (2020), to generate model spectra.

In each case, we bin the resulting model transmission spectrum to the resolution of the data before performing a reduced- χ^2 comparison. The full datasets of all

three reductions to which we fit our forward models and retrievals can be found with the Supplemental Materials. As with the Gaussian hypothesis tests, we exclude the data points in the grey shaded region of Figure 2 from our model-fitting due to steeply-falling instrument throughput at these wavelengths (< 2.87).

As shown in Figure 3, the slight slope and flatness of the spectra from each reduction allow us to confidently disregard low mean molecular weight atmospheres dominated by hydrogen/helium – up to metallicities of $1000\times$ solar – to greater than 3σ . This improves upon the previous high resolution data obtained by Ridden-Harper et al. (2022) that could only strongly rule out atmospheres up to a few times solar. Our $1000\times$ solar metallicity atmosphere has an average mean molecular weight of 13.86 g/mol compared to the high resolution’s 5 g/mol limit, though our constraint is less stringent for non-chemically consistent atmospheres (see Section 4.3).

Fig. Set 3. Atmospheric Forward Models compared to Data

We also compare the data from each reduction to a set of end-member forward models from PICASO with single-gas 1 bar, isothermal atmospheres. For ease of interpretation, we focus here on the results from the **Eureka!** reduction, as we determined that it was the most representative dataset, with the smallest weighted average deviation from the median of all three reductions. However, the trend in best-fit agrees among all

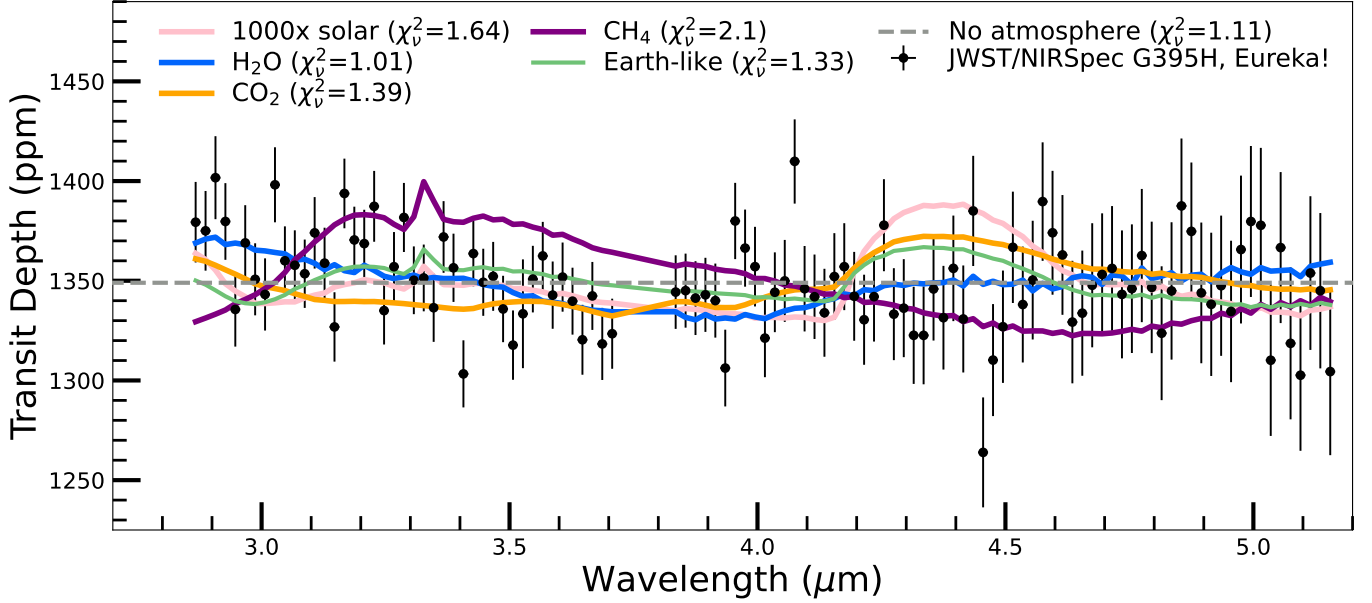


Figure 3. Our final *Eureka!* spectra of GJ 486b binned to $R \sim 200$ (black points) compared to a set of *PICASO* forward models (colored lines: 1000 \times solar, pink; H_2O , blue; CO_2 , orange; CH_4 , purple; Earth-composition, green). A 1 bar, pure water atmosphere on GJ 486b fits the data with the lowest reduced- χ^2 (1.01), and a flat-line model (dashed grey line) is nearly as well fit by the data (reduced- $\chi^2 = 1.11$), though is weakly rejected by Gaussian vs flat line tests. Alternatively, stellar contamination with water in the atmosphere of the star, rather than the planet, can explain the observed transit depths (see Fig. 4).

three reductions (for a complete description of each reduction’s fit, see Table 5 in Appendix C). The slight slope on the blue end of NRS1 results in best-fitting (reduced- $\chi^2 = 1.01$) forward models that contain pure water vapor, as this molecule has a strong absorption feature from 2.2 to 3.7 μm , consistent with the slope we observe in NRS1.

Our data across all reductions also moderately to weakly rule out carbon-rich atmospheres of either CH_4 or CO_2 to 6.5σ and 2.3σ , respectively. A flat-line model, representative of an airless body or a high-altitude (0.1 μbar) cloud deck, fit the data with reduced- $\chi^2 = 1.11$, which is statistically equivalent to the clear water atmosphere model within the forward modeling framework. However, between its equilibrium temperature and size, GJ 486b is not expected to support clouds to such low pressures, as there are few condensible species in this temperature range. Photochemical hazes could dampen the presence of any spectral features with a haze layer at this altitude and create a flat line spectrum (Gao et al. 2020; Pidhorodetska et al. 2021; Caballero et al. 2022); however, given the Bayesian evidence of the Gaussian absorption tests discussed above, the water atmosphere is the preferred explanation from the *PICASO* analysis for all reductions. We note that the *FIREFLY* reduction only weakly rejects the flat line hypothesis and, therefore, an airless planet or very hazy planet is still a possibility. In Figure 3, we show the results of our *PICASO* forward

modeling compared to the *Eureka!* data. The full set of results for each reduction is available in the online journal.

4.3. Retrievals Suggest a Water-rich Atmosphere or Unocculted Starspot Contamination

In addition to our forward model comparisons, we performed an atmospheric retrieval analysis to assess the robustness of our tentative evidence for a water-rich atmosphere and consider alternative astrophysical explanations. We apply two independent retrieval codes — *POSEIDON* (MacDonald & Madhusudhan 2017; MacDonald 2023) and *rfast* (Robinson & Salvador 2023) — to all three data reductions to ensure reliable inferences.

4.3.1. Water-rich Atmosphere Scenario

Our *POSEIDON* atmospheric retrieval considers six potential gases that can range in abundance from being trace volatiles to the dominant background gas: N_2 , H_2 , H_2O , CH_4 , CO_2 , and CO . The opacity contributions from these gases include line opacity (Polyansky et al. 2018; Yurchenko et al. 2017; Tashkun & Perevalov 2011; Li et al. 2015) and collision-induced absorption (CIA) from $\text{H}_2\text{-H}_2$, $\text{H}_2\text{-N}_2$, $\text{H}_2\text{-CH}_4$, $\text{H}_2\text{-CO}_2$, $\text{CO}_2\text{-CO}_2$, $\text{CO}_2\text{-CH}_4$, and $\text{N}_2\text{-N}_2$ (Karman et al. 2019). Since the mixing ratios must sum to unity, we have five free parameters describing their mixing ratios that each follow centered log-ratio (CLR) priors, ranging from 10^{-12} to 1, as described by Lustig-Yaeger & Fu et al. (2023).

The other free parameters are the isothermal temperature (\mathcal{U} [200 K, 900 K]), the atmosphere radius at the 1 bar reference pressure (\mathcal{U} [$0.9 R_{p, \text{obs}}$, $1.1 R_{p, \text{obs}}$]), and the log-pressure of an opaque surface (\mathcal{U} [-7, 2], in bar). We calculate transmission spectra via opacity sampling at a resolving power of $R = 20,000$ from $0.5\text{--}5.4\ \mu\text{m}$, with the lower wavelength limit set far below our shortest wavelength ($2.8\ \mu\text{m}$) to later demonstrate how retrieval solutions diverge at optical wavelengths. These 8-parameter POSEIDON retrievals used the PyMultiNest (Feroz et al. 2009; Buchner et al. 2014) package to explore the parameter space with 2,000 live points.

Fig. Set 4. Retrieval of GJ 486b’s Transmission Spectrum

Figure 4 shows our POSEIDON retrieval results for this atmospheric model scenario (blue retrieved spectrum and histograms) for the Eureka! data reduction – see the online figure set for the other two reductions. For Eureka! and FIREFLY, the preferred explanation for the observed rise in the blue wavelengths of the transmission spectrum is H_2O opacity from the wing of the band centered on $2.8\ \mu\text{m}$. Bayesian model comparisons favor the presence of H_2O with Bayes factors of 133 and 8 (3.6σ and 2.6σ) for Eureka! and FIREFLY, respectively. The retrieved H_2O abundance posterior indicates that water is the most likely background gas (e.g., Eureka! requires a H_2O mixing ratio $> 10\%$ to 2σ confidence), with an upper limit ruling out a H_2 -dominated atmosphere. The Eureka! and Tiberius reductions also yield upper limits on the CH_4 and CO_2 abundances (see the Appendix, Figure 6). The Tiberius reduction, however, does not uniquely infer a water-rich atmosphere. Though a water-rich atmosphere remains the preferred solution for Tiberius, a secondary mode permits a clear, H_2 -dominated atmosphere with no other gases contributing to the spectrum. This secondary mode reflects a solution where the wavelength dependence of $\text{H}_2\text{--H}_2$ CIA is used to fit the spectrum. This solution is unphysical since an H_2 -dominated atmosphere will always contain other trace molecules with more prominent absorption features at these wavelengths. Upon further investigation, we found that the unphysical solution is driven by the upwards rise at the longest wavelengths that are only present in the Tiberius reduction (see Figure 2). We, therefore, conclude that a consistent explanation for GJ 486b’s transmission spectrum, assuming the observed non-flatness is caused by atmospheric absorption, can be readily explained ($\chi^2_\nu \approx 1.0$) by a water-rich atmosphere — in agreement with the forward models in Section 4.2.

We also conducted single-composition atmospheric retrievals with **rfast** for all three reductions. These re-

trievals consider atmospheres with a single absorbing gas alongside a spectrally inactive background gas with an agnostic mean molecular weight. Our **rfast** retrieval model has 6 free parameters: the log-gas mixing ratio, $\log_{10} f_{\text{gas}}$ (\mathcal{U} [-12, 0]), the log-surface pressure, $\log_{10} P_0$ (\mathcal{U} [-1, 6], in Pa), the surface temperature, T_0 (\mathcal{U} [300, 1100] K), the mean molecular weight of the background gas, m_b (\mathcal{U} [2, 50] amu), the planet radius, R_p (\mathcal{U} [$1.1, 1.4 R_\oplus$]), and the planet mass, M_p (\mathcal{N} [2.28, 0.12] M_\oplus). For the single gases, we consider, in separate retrievals, H_2O , CO_2 , CO , and CH_4 . The **rfast** retrievals use **emcee** (Foreman-Mackey et al. 2013) with 100 walkers for 15,000 steps, where the first 5,000 are discarded for burn-in.

We show our **rfast** 1D posteriors in the Appendix (Figure 7). Our **rfast** retrievals also identify a H_2O -rich atmosphere as a consistent explanation for the Eureka! and FIREFLY reductions (though the lower limits on H_2O are weaker compared with POSEIDON due to the combination of a free mean molecular weight, planet mass, and log-uniform vs. CLR priors). **rfast** also finds that the Tiberius reduction permits lower mean-molecular weight atmospheres for similar reasons to POSEIDON.

4.3.2. Unocculted Starspot Scenario

We now consider the potential for GJ 486b’s host star alone to explain our observed transmission spectrum. Stellar heterogeneities (starspots and/or faculae) that are not occulted during transit can induce wavelength-dependent features in transmission spectra if the stellar intensity illuminating the planetary atmosphere differs from the overall average stellar intensity — also known as the transit light source effect (TLS) (e.g., Rackham et al. 2018). This confounding stellar influence is a crucial consideration for transmission spectra of planets orbiting cool M dwarfs, such as GJ 486, since H_2O existing in cold starspots could mimic atmospheric signatures.

We implement stellar contamination retrievals with POSEIDON following a similar approach to Rathcke et al. (2021), based on the parameterization from Pinhas et al. (2018). The contamination model is defined by four parameters: the stellar heterogeneity temperature, T_{het} (\mathcal{U} [2300 K, $1.2 T_{*, \text{eff}}$]), the heterogeneity coverage fraction, f_{het} (\mathcal{U} [0, 0.5]), the stellar photosphere temperature, T_{phot} (\mathcal{N} [$T_{*, \text{eff}}$, $\sigma_{T_{*, \text{eff}}}$]), and the planetary radius, R_p (\mathcal{U} [$0.9 R_{p, \text{obs}}$, $1.1 R_{p, \text{obs}}$]). For the priors, we adopt literature values of $T_{*, \text{eff}} = 3340$ K and $\sigma_{T_{*, \text{eff}}} = 54$ K (Trifonov et al. 2021). We calculate the stellar contamination factor by interpolating the Allard et al. (2012) grid of stellar PHOENIX models using the pysynphot package (STScI Development Team 2013).

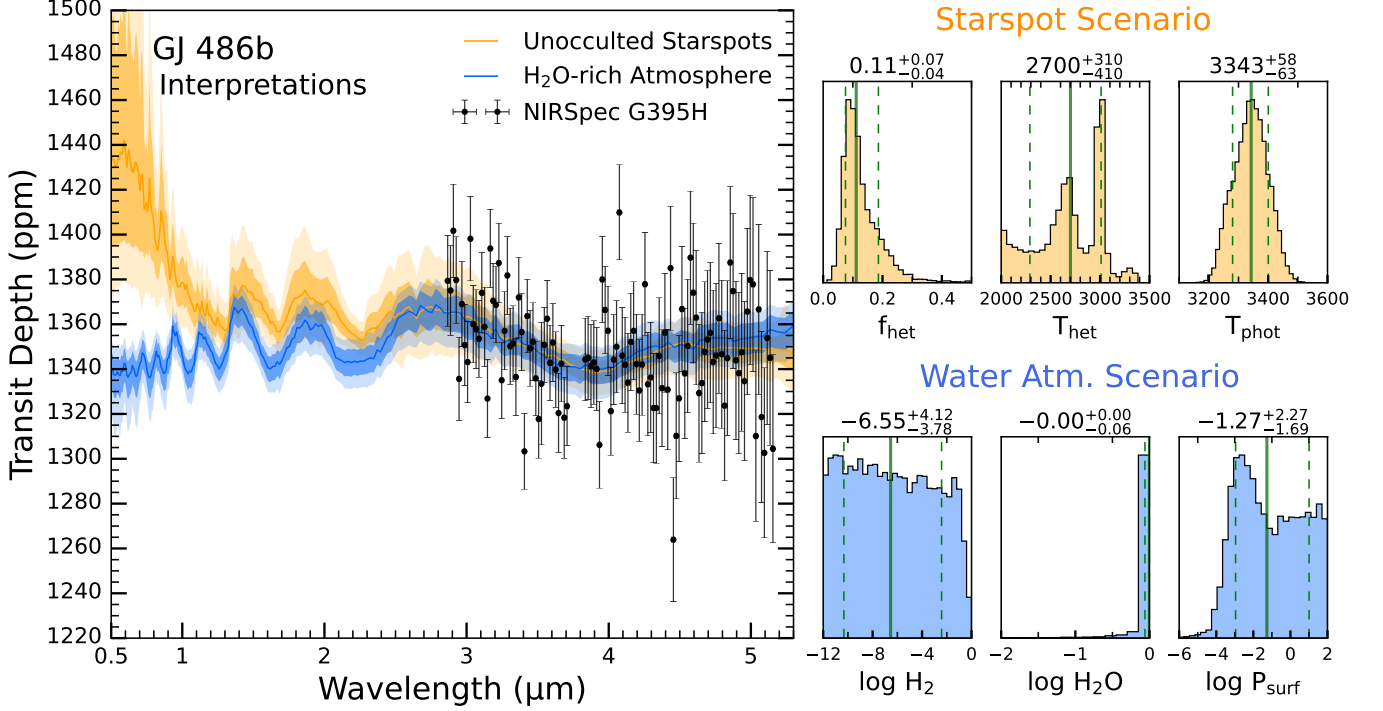


Figure 4. POSEIDON retrieval results for GJ 486b’s transmission spectrum. Left: retrieved transmission spectra for two models compared to the *JWST* NIRSpec G395H data from the *Eureka!* reduction (black points with error bars). Two scenarios can equivalently explain GJ 486b’s transmission spectrum ($\chi^2_\nu = 1.0$): unocculted starspots with no planetary atmosphere (orange contours) or a water-rich atmosphere with no starspots (blue contours). The median retrieved spectrum (solid lines) and 1 σ and 2 σ confidence intervals (dark and light contours) for each scenario are overlaid. Top right: posterior histograms for the unocculted starspot model, defined by the fractional coverage area of cold stellar heterogeneities/spots (f_{het}), the temperature of the heterogeneities/spots (T_{het}), and the stellar photospheric temperature (T_{phot}). Bottom right: posterior histogram for the water-rich atmosphere scenario, highlighting hydrogen and water’s retrieved mixing ratios alongside the atmospheric surface pressure. Water is necessary to explain GJ 486b’s spectrum, but the retrievals cannot differentiate between a water-rich planetary atmosphere or water contained in cool starspots that contaminate the transmission spectrum. The complete figure set (3 images, one for each reduction) is available in the online journal.

Figure 4 demonstrates that contamination from unocculted starspots, with no planetary atmosphere, provides an equally plausible ($\chi^2_\nu \approx 1.0$) alternative explanation to GJ 486b’s transmission spectrum. In this scenario, the observed slope in the spectrum is still caused by the wing of an H₂O band, but the water resides in the host star. The POSEIDON retrievals for all three data reductions yield a spot coverage fraction of $\sim 10\%$, but with relatively weak and inconsistent constraints on the spot temperature. Compared to a flat spectrum, the unocculted starspot model is preferred with Bayes factors of 255, 16, and 114 (3.8 σ , 2.9 σ , and 3.5 σ) for *Eureka!*, *FIREFLY*, and *Tiberius*, respectively. We stress that, while our present observations cannot distinguish between the water-rich atmosphere scenario and unocculted starspots, these two scenarios deviate substantially at shorter wavelengths (see Figure 4). Consequently, even in the case of aerosol-laden atmospheres (Rackham et al. 2022), future observations at shorter

wavelengths can readily distinguish which scenario is correct.

4.4. A Spotty Star Best Explains the Stellar Spectrum

To further investigate the possibility of stellar contamination, we return to the *JWST*/NIRSpec G395H data to probe the Stage 3 stellar spectra and examine whether the star is consistent with a particular stellar model. Upon completing Stage 2 of the *jwst* pipeline with the flat fielding and absolute photometric calibration steps enabled, we noticed that only the region within 8 pixels of the trace is converted to units of M.Jy. The remaining pixel regions are in DN/s, so we manually mask them before running Stage 3 of *Eureka!*. Due to the lack of unmasked background pixels, we disable Stage 3 background subtraction for this flux-calibrated reduction. This change does not skew the final calibrated spectrum since we already performed group-level background subtraction in Stage 1.

To compute the stellar baseline spectrum, we exclude 1040 integrations during transit (1560 - 2599) and then compute median values along the time axis. We manually mask a few obvious outliers before estimating the baseline spectrum uncertainties by computing the standard deviation in flux along the time axis. Typical uncertainties are 3 – 5 mJy, but can be as large as 55 mJy for some spectral channels. The typical uncertainty values are consistent with the uncertainties derived from our standard spectral extraction routine. We do not use the standard error calculation for our uncertainties. That is, we do not divide our uncertainties by the square root of the number of integrations because, as demonstrated below, the standard deviation in flux better represents the true uncertainty in our flux-calibrated spectrum. We note that the derived baseline spectrum is remarkably consistent between both transits (see Figure 5).

We used PHOENIX stellar models produced by Allard et al. (2012) to analyze whether the observed stellar baseline spectrum is best explained by a spotless or spotted star. We utilized the Allard et al. (2012) models, as in Section 4.3.2, because they account for the formation of molecular bands including H₂O, CH₄, and TiO₂ and have higher ($\Delta\lambda=2$ Å) resolution than the observations. This grid of models also has sufficient temperature and gravity coverage to model the photospheres of M-dwarf stars and their spots and faculae ($T_{\text{eff}} \geq 2000$ K, $\log(g) = 0 - 6$ cm s⁻²).

We employed single PHOENIX models to represent spotless (or one-component) stars. We used weighted linear combinations of PHOENIX models to create inhomogeneous models. Two-component models include one model with $T_{\text{eff}} \geq 3000$ K to represent the background photosphere and a second, cooler model with $T_{\text{eff}} \leq T_{\text{eff,photosphere}} - 100$ K to represent spots. Three-component models include an additional $T_{\text{eff}} \geq T_{\text{eff,photosphere}} + 100$ K model to represent faculae. In the two- and three-component models, all spots have the same T_{eff} and $\log(g)$, as do the faculae. Linear combinations were computed by interpolating the spot and faculae models onto the photosphere wavelength grid before summing the fluxes in a weighted fraction where the photosphere was required to be $\geq 50\%$ of the total.

To compare the models to the observed baseline spectra, we converted the native wavelengths from Å to μm and the flux densities from ergs s⁻¹ cm⁻² cm⁻¹ to fluxes in units of mJy. We then scaled the models by R_*^2/dist^2 using literature values for GJ 486: $R_*=0.33 R_\odot$ (Trifonov et al. 2021) and $\text{dist} = 8.07$ pc (Gaia Collaboration et al. 2021). We smoothed and interpolated the models to be the same resolution as the observations before cal-

culating a reduced- χ^2 . In our reduced- χ^2 calculations, we considered 3187 wavelength points for Transit 1 (3180 for Transit 2) and three fitted parameters (T_{eff} , $\log(g)$, and a scaling factor). The multi-component models included additional fit parameters for determining the percent coverage for the spots and faculae. The scaling factor was multiplied by the R_*^2/dist^2 term to account for uncertainty in either measured quantity and varied from 0.9 to 1.1. To get the final reduced- χ^2 value for each model, we computed reduced- χ^2 individually for Transits 1 and 2 and then took the average.

Considering each type of one-, two-, and three-component model individually, we find that the models with the smallest reduced- χ^2 values are fairly consistent with the existing literature values, though no model is a particularly good fit with a reduced- χ^2 near 1 (for numerical details, see Appendix B). A 100% $T_{\text{eff}} = 3300$ K, $\log(g)=4.5$ cgs model with $\chi_\nu^2=72.0$ is the preferred one-component photosphere model (scale factor = 1.05), yielding a lower surface gravity than expected for a field age mid-M-dwarf like GJ 486. In agreement with our updated $\log(g)=4.91\pm0.02$ cgs, we disfavor the low stellar surface gravity of the best-matched photosphere-only model when taking into account inhomogeneities on the stellar surface. A 75% $T_{\text{eff}} = 3400$ K, $\log(g)=5$ cgs background photosphere with 25% spot coverage at $T_{\text{eff}} = 3000$ K, $\log(g)=5$ cgs is the preferred two-component model ($\chi_\nu^2=53.4$; scale factor = 1.05). The model most preferred overall is a three-component model with $\chi_\nu^2=49.0$ that has a background photosphere with $T_{\text{eff}} = 3200$ K, $\log(g)=5$ cgs, 20% spot coverage at $T_{\text{eff}} = 3000$ K, $\log(g)=5$ cgs, and 25% faculae coverage at $T_{\text{eff}} = 3400$ K, $\log(g)=5$ cgs (scale factor = 1.1). These three models are shown in Figure 5 compared to the Baseline GJ 486 spectra from Transits 1 and 2. There is decent general agreement for each model throughout the full $\sim 2.9\text{--}5$ μm range, with slightly better agreement for the three-component photosphere+spot+faculae model, indicating that we cannot rule out star spots as a source for the presumed water detection.

5. DISCUSSION AND CONCLUSIONS

There is remarkable agreement in the stellar heterogeneity parameters obtained from a) retrieving for occulted star spots in the planetary transmission spectrum and b) fitting the baseline stellar spectrum with PHOENIX multi-component stellar models. Both lines of inquiry find best fits with overlapping values for faculae/spot coverage and temperature as well as the photospheric temperature. The stellar spectrum is best fit by a 3200 K photosphere with 20% cool spots at 3000 K and 25% hot faculae at 3400 K. These values match

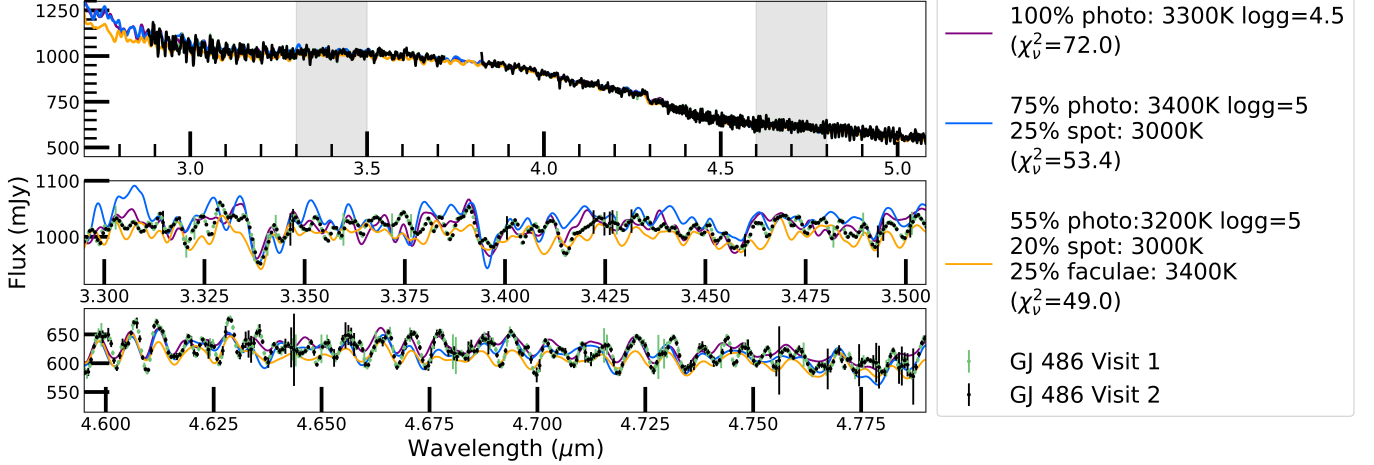


Figure 5. Best matching one-, two-, and three-component PHOENIX models to the Baseline GJ 486 spectra from Transits 1 (green) and 2 (black). The bottom two panels zoom-in on the grey highlighted regions of the top panel spectrum. When considering a one-component photosphere, a $T_{\text{eff}} = 3300$ K, $\log(g)=4.5$ cgs model is preferred (purple, $\chi^2_{\nu} = 72.0$). When allowing for spots in a two-component model, a warmer $T_{\text{eff}} = 3400$ K, $\log(g)=5$ cgs photosphere with 25% coverage of $T_{\text{eff}} = 3000$ K, $\log(g)=5$ cgs spots is the preferred model (blue, $\chi^2_{\nu} = 53.4$). The best overall match to the observations is produced with a three-component photosphere+spots+faculae model that has a background photosphere with $T_{\text{eff}} = 3200$ K, $\log(g)=5$ cgs, 20% spot coverage ($T_{\text{eff}} = 3000$ K, $\log(g)=5$ cgs), and 25% faculae coverage ($T_{\text{eff}} = 3400$ K, $\log(g)=5$ cgs) (orange, $\chi^2_{\nu} = 49.0$).

well compared to the TLS retrievals with a 3280 K photospheric temperature lower limit and cool spots up to ~ 3100 K at 7 - 18% coverage (see Figure 6). This consistency lends strong support to this physical interpretation of our JWST NIRSpec/G395H data. Moreover, even quiescent M dwarfs are known to be highly heterogeneous with strong impacts on the transmission spectrum (Rackham et al. 2018; Zhang et al. 2018; Somers et al. 2020).

Our forward model water atmosphere demonstrates that water is the best-fit absorber to explain GJ 486b’s spectrum in the absence of stellar contamination. Such a pure steam atmosphere could theoretically be generated by impacts from small, icy bodies (Zahnle et al. 1988) or outgassed depending on the mantle composition (Tian & Heng 2023), but would be quickly lost via the runaway greenhouse effect (Goldblatt et al. 2013), as well as being disfavored by high resolution observations (Ridden-Harper et al. 2022). We examine the effect of adding CO₂ to our H₂O forward model, finding that scaling the carbon content upwards always results in a worse fit to the data. In the water-rich POSEIDON retrievals, we find strong water abundance lower limits across the three reductions, with an agnostic background gas prior. Two carbon species have stringent upper limits: carbon dioxide and methane. All reductions have posteriors where the constrained carbon species abundances can supersede that of water, but the best fits prefer atmospheres where water vapor dominates over carbon species. Such atmospheres would be challenging

to maintain at GJ 486b’s 700 K equilibrium temperature, given our current understanding of the runaway greenhouse effect (Goldblatt et al. 2013) and expected limits on the interior sequestration and outgassing rates of carbon species relative to water (Sossi et al. 2023; Tian & Heng 2023). However, given the large range of retrieved abundances compatible with GJ 486’s spectrum, they remain consistent with atmospheric theory. Furthermore, our retrievals cannot constrain the abundance of carbon monoxide (CO), providing an additional potential reservoir for carbon in the atmosphere. A warm, water-rich atmosphere with little atmospheric carbon would represent a terrestrial exoplanet wholly unlike any solar system analogue and challenge our understanding of atmospheric formation (Wordsworth & Kreidberg 2022; McIntyre et al. 2023).

GJ 486b joins the ranks of other terrestrial M-dwarf planets with tantalizing atmospheric inferences. Such planets include the first planet of our JWST-GO-1981 program, LHS 475b, exisiting observations of which cannot distinguish a carbon dioxide atmosphere from an airless body (Lustig-Yaeger et al. 2023). L 98-59c is another planet where recent HST observations have tentatively suggested either a hydrogen-rich planetary atmosphere or stellar contamination (Barclay et al. 2023) — though a different analysis favored a flat, featureless transmission spectrum (Zhou et al. 2023). Both GJ 486b at 1.3 R_⊕ and L 98-59c at 1.35 R_⊕ track the upper edge of planets below the expected hydrogen-dominated atmospheric cut-off (Rogers 2015; Rogers et al. 2021).

786 Their difference in insolation, with GJ 486b at $T_{\text{eq}} =$
 787 700 K and L 98-59c at $T_{\text{eq}} = 550$ K, combined with
 788 their retrieved upper limit atmospheric hydrogen frac-
 789 tions, offer suggestive hints at a cosmic shoreline that
 790 is confounded by potential stellar contamination. More
 791 data is clearly necessary to confidently mark the bound-
 792 aries of any cosmic shoreline.

793 Secondary eclipse observations of GJ 486b with
 794 *JWST*'s Mid-Infrared Instrument (MIRI) Low Resolu-
 795 tion Spectroscopy (LRS) mode are already scheduled
 796 (GO 1743, PI: Mansfield). These observations will mea-
 797 sure the dayside emission spectrum of the planet, al-
 798 lowing an expected 5σ constraint on surface pressures
 799 ≥ 1 bar, as well as providing evidence for the atmo-
 800 spheric composition with a sufficiently thick atmosphere
 801 (Mansfield et al. 2019, 2021). Thus, these MIRI/LRS
 802 observations can lend an additional line of evidence for
 803 or against both a significant atmosphere as well as the
 804 presence of water. However, our water-rich atmospheric
 805 retrieval scenario demonstrates that much lower surface
 806 pressures (down to millibar levels) are consistent with
 807 the data from NIRSpec/G395H, which is beyond the
 808 sensitivity of the planned MIRI/LRS observations. In
 809 this case, the secondary eclipse emission spectrum is un-
 810 likely to provide strong evidence in favor of either of our
 811 interpretations for GJ 486b.

812 As seen in Figure 4, the unocculted star spot scenario
 813 and the water-rich atmosphere scenario diverge strongly
 814 shortwards of $0.8 \mu\text{m}$. In the case that the upcoming
 815 MIRI observations cannot definitely detect an atmo-
 816 sphere, high precision shorter wavelength observations
 817 could provide evidence for or against an atmosphere on
 818 GJ 486b. Ultimately, our *JWST* NIRSpec/G395H stel-
 819 lar and transmission spectra, combined with retrievals
 820 and stellar models, suggest either an airless planet with
 821 a spotted host star or a significant planetary atmosphere
 822 containing water vapor. Given the agreement between
 823 our stellar modeling and atmospheric retrievals for the
 824 spot scenario, this interpretation may have a slight edge
 825 over a water-rich atmosphere. However, a true determi-
 826 nation of the nature of GJ 486b remains on the horizon,
 827 with wider wavelength observations holding the key to
 828 this world's location along the cosmic shoreline.

829 We thank the anonymous referee whose comments im-
 830 proved this manuscript. This work is based in part on
 831 observations made with the NASA/ESA/CSA *JWST*.
 832 The data were obtained from the Mikulski Archive for
 833 Space Telescopes at the Space Telescope Science Insti-
 834 tute, which is operated by the Association of Universi-
 835 ties for Research in Astronomy, Inc., under NASA con-
 836 tract NAS 5-03127 for *JWST*. These observations are
 837 associated with program #1981. Support for program
 838 #1981 was provided by NASA through a grant from
 839 the Space Telescope Science Institute, which is oper-
 840 ated by the Association of Universities for Research in
 841 Astronomy, Inc., under NASA contract NAS 5-03127.
 842 This material is based in part upon work performed
 843 as part of the CHAMPs (Consortium on Habitability
 844 and Atmospheres of M-dwarf Planets) team, supported
 845 by the National Aeronautics and Space Administra-
 846 tion (NASA) under Grant No. 80NSSC21K0905 issued
 847 through the Interdisciplinary Consortia for Astrobiol-
 848 ogy Research (ICAR) program. The material is based
 849 upon work supported by NASA under award number
 850 80GSFC21M0002. We also acknowledge Jordin Sparks
 851 for her lyrical genius.

852 *Facilities:* *JWST*(NIRSpec) All the *JWST* data
 853 used in this paper can be found in MAST:
 854 [10.17909/z89v-dg97](https://mast.stsci.edu/portal/#doc/10.17909/z89v-dg97).

855 *Software:* Astropy (Astropy Collaboration et al.
 856 2013, 2018), batman (Kreidberg 2015), CHIMERA (Line
 857 & Yung 2013; Line et al. 2014), Dynesty (Speagle 2020),
 858 emcee (Foreman-Mackey et al. 2013), Eureka! (Bell et al.
 859 2022), ExoCTK (Bourque et al. 2021), FIREFLY (Rus-
 860 tamkulov et al. 2022), Forecaster (Chen & Kipping
 861 2017), IPython (Pérez & Granger 2007), jwst (Bushouse
 862 et al. 2022), Matplotlib (Hunter 2007), NumPy (van der
 863 Walt et al. 2011; Harris et al. 2020), PHOENIX (Allard
 864 et al. 2012) PICASO (Batalha et al. 2019), POSEIDON
 865 (MacDonald & Madhusudhan 2017; MacDonald 2023),
 866 PyMC3 (Salvatier et al. 2016), pysynphot(STScI Devel-
 867 opment Team 2013), rfast (Robinson & Salvador 2023),
 868 SciPy (Virtanen et al. 2020), Tiberius (Kirk et al. 2019,
 869 2021)

APPENDIX

A. DATA REDUCTION

Dataset	T_0 (BJD _{TDB})	i (°)	a/R_{s*}	R_P/R_*	Residual RMS (ppm)
Transit 1, NRS1	2459939.071619 ^{+2.0e-05} _{-2.1e-05}	89.10 ^{+0.26} _{-0.35}	11.24 ^{+0.03} _{-0.09}	0.03697 ± 0.00009	143
Transit 1, NRS2	2459939.071570 ^{+2.4e-05} _{-2.4e-05}	89.06 ^{+0.34} _{-0.38}	11.22 ^{+0.06} _{-0.13}	0.03784 ± 0.00009	171
Transit 2, NRS1	2459943.472959 ^{+2.0e-05} _{-2.0e-05}	89.02 ^{+0.35} _{-0.38}	11.23 ^{+0.07} _{-0.13}	0.03689 ± 0.00009	137
Transit 2, NRS2	2459943.472974 ^{+2.3e-05} _{-2.4e-05}	89.06 ^{+0.46} _{-0.47}	11.22 ^{+0.10} _{-0.19}	0.03670 ± 0.00009	158
Weighted Mean	2459939.071594 ± 1.6e-05 2459943.472967 ± 1.5e-05	89.06 ± 0.18	11.229 ± 0.043	0.03709 ± 0.00004	n/a

Table 1. Best-fit system parameters and 1 σ uncertainties from fitting the four white light curves using **Eureka**!

Dataset	T_0 (BJD _{TDB})	i (°)	a/R_{s*}	R_P/R_*	Residual RMS (ppm)
Transit 1, NRS1	2459939.0716102 ± 2.1e-05	89.11 ± 0.35	11.294 ± 0.137	0.03759 ± 0.00013	132
Transit 1, NRS2	2459939.0715592 ± 2.2e-05	89.97 ± 0.27	11.449 ± 0.023	0.03791 ± 0.00010	159
Transit 2, NRS1	2459943.4729689 ± 1.9e-05	89.99 ± 0.22	11.446 ± 0.021	0.03784 ± 0.00013	130
Transit 2, NRS2	2459943.4730019 ± 2.3e-05	89.30 ± 0.40	11.325 ± 0.111	0.03742 ± 0.00017	158
Weighted Mean	2459939.0715859 ± 1.5e-05 2459943.4729823 ± 1.5e-05	89.75 ± 0.14	11.443 ± 0.015	0.03775 ± 0.000063	n/a

Table 2. The system parameters resulting from the **FIREFLY** fits to the white light curves.

Dataset	T_0 (BJD _{TDB})	i (°)	a/R_{s*}	R_P/R_*	Residual RMS (ppm)
Transit 1, NRS1	2459939.071586 ^{+3.5e-05} _{-3.6e-05}	89.99 ^{+0.65} _{-0.61}	11.34 ^{+0.04} _{-0.13}	0.03683 ± 0.00015	158
Transit 1, NRS2	2459939.071548 ^{+3.6e-05} _{-3.5e-05}	89.97 ^{+0.67} _{-0.62}	11.36 ^{+0.05} _{-0.13}	0.03756 ± 0.00017	188
Transit 2, NRS1	2459943.472952 ^{+3.6e-05} _{-3.5e-05}	90.02 ^{+0.75} _{-0.72}	11.42 ^{+0.06} _{-0.17}	0.03684 ± 0.00015	158
Transit 2, NRS2	2459943.472955 ^{+4.3e-05} _{-4.3e-05}	89.83 ^{+1.35} _{-1.32}	11.23 ^{+0.19} _{-0.4}	0.03685 ± 0.00019	194
Weighted Mean	2459939.07158 ± 1.9e-05	89.96 ± 0.37	11.40 ± 0.06	0.03701 ± 8e-05	n/a

Table 3. The system parameters resulting from the **Tiberius** fits to the white light curves.

A.1. Data Reduction Consistency: An Offset between the NRS1 and NRS2 Detectors

As stated in the main text, all initial reductions showed a consistent offset in measured transit depth for the Transit 1, NRS2 detector relative to the other white light curve depths. Since this shift is not seen in the NRS1 detector, we can confidently rule out all astrophysical effects (e.g., stellar variability) as a source of the discrepancy. For the **FIREFLY** reduction, we altered our application of the superbias in the bias subtraction step and light-curve fitting stages, which we found produced more consistent transit depths for NRS1 and NRS2.

In our **FIREFLY** reduction, we measured the superbias level by rescaling the superbias image to match the level in the trace-masked groups of each integration. We note that a full readout of the detector mitigates bias drifts using reference pixels, but the subarray readouts used here do not have such pixels. We find that the superbias level changes by hundreds of ppm throughout the time series, with typical values of the scaling factor about 1.003. We use the standard-deviation-normalized time series of the superbias scaling coefficient as a detrending vector at the light-curve fitting stage, added linearly to our usual systematics model. We find that the superbias decorrelation coefficient is statistically preferred in the systematics model, with some residual structure in the photometry well-explained by this

term. The addition of superbias detrending reduced the transit depth tension between NRS1 and NRS2, with the white-light curve transit depths agreeing within the uncertainties.

For the **Eureka!** reduction, we also investigated time-dependent variations in the NRS2 detector bias level. We found that applying a scale factor correction to the superbias frame for each integration in Stage 1 marginally improved the consistency in measured transit depths (by ~ 20 ppm), but also led to increased scatter. Applying a single scale factor correction for all integrations yielded a similar improvement, but without the increased scatter. We continue to investigate different methods of scaling the superbias frame. In the meantime, we elect to adopt the standard bias correction in our final **Eureka!** analysis and apply a manual offset of 78 ppm in transit depth to NRS2, Transit 1.

To account for NRS2 transit visit discrepancy for the final **Tiberius** reduction, we also manually offset the transmission spectrum for NRS2, Transit 1 by 63 ppm, such that the median transit depth was equal to NRS2, Transit 2.

After this superbias-detrending in **FIREFLY** and manual offsets in **Eureka!** and **Tiberius**, we saw excellent agreement between the **Eureka!**, **FIREFLY**, and **Tiberius** spectra across both NRS1 and NRS2 in both transits, as shown in Figure 2. Since the superbias correction alters **FIREFLY**’s absolute transit depths, we elect to compare their relative transit depths.

B. STELLAR MODEL STATISTICS

Model Configuration	χ^2_ν	χ^2	n	K
Photosphere	72.0	228,680.81	3,187	3
Photosphere+Spot	53.4	169,489.64	3,187	5
Photosphere+Spot+Faculae	49.0	155,374.94	3,187	7

Table 4. Summary of values for our goodness-of-fit testing, where n is the number of wavelength points, and K is the number of free parameters.

C. INTERPRETATION SUPPLEMENTAL INFORMATION

CHIMERA Forward Model	Eureka! (dof = 110)	FIREFLY (dof = 46)	Tiberius (dof = 46)	Average σ ruled out	Significance
1000 \times solar	1.64	1.26	2.44	3.6	moderately ruled out
H ₂ O, 1 bar	1.01	0.76	1.37	0.9	consistent with data
CO ₂ , 1 bar	1.39	1.17	1.63	2.3	weakly/moderately ruled out
CH ₄ , 1 bar	2.10	1.77	5.96	6.5	strongly ruled out
Earth-like	1.33	1.04	2.35	2.8	moderately ruled out
Flat line	1.11	0.91	1.60	1.5	weakly/moderately rejected by Gaussian fitting

Table 5. Each reduction’s reduced- χ^2 compared to our end-member composition **PICASO** forward models. Since each reduction has a different degree-of-freedom (dof), we also report the average significance (in σ , following Trotta (2017)) by which the model is ruled out. Note that the “flat line” model can correspond either to an airless planet or a very hazy atmosphere.

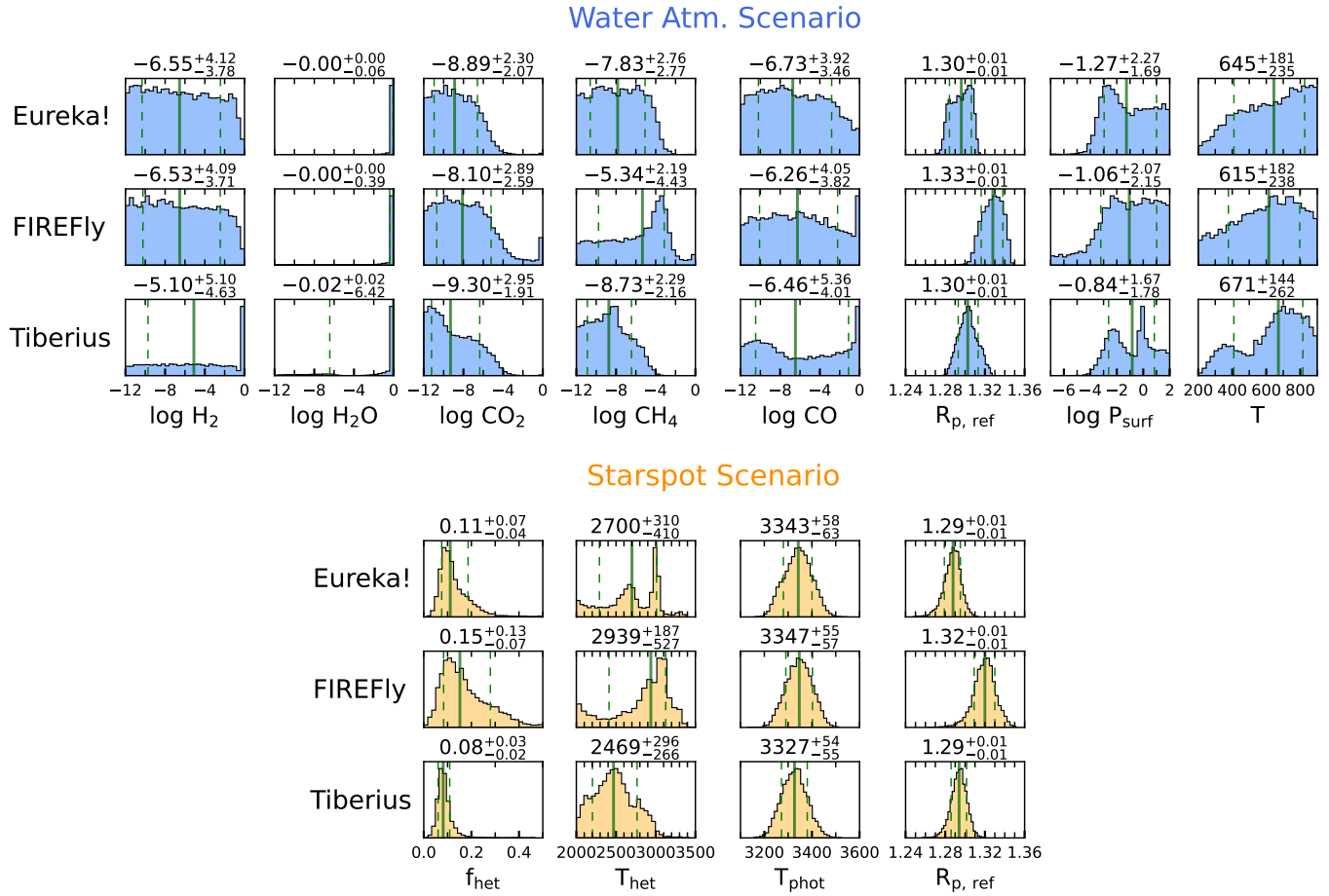


Figure 6. Posterior probability distributions from the POSEIDON retrievals. Top rows (blue): retrieval model where GJ 486b's spectrum is caused by a water-rich atmosphere. Bottom rows (orange): retrieval model instead considering unocculted starspots. The rows in each scenario correspond to different data reductions (Eureka!, FIREFLY, and Tiberius from top to bottom).

REFERENCES

- 902 Airapetian, V. S., Gloer, A., Khazanov, G. V., et al. 2017,
 903 ApJL, 836, L3, doi: [10.3847/2041-8213/836/1/L3](https://doi.org/10.3847/2041-8213/836/1/L3)
 904 Airapetian, V. S., Barnes, R., Cohen, O., et al. 2020,
 905 International Journal of Astrobiology, 19, 136,
 906 doi: [10.1017/S1473550419000132](https://doi.org/10.1017/S1473550419000132)
 907 Allard, F., Homeier, D., & Freytag, B. 2012, Philosophical
 908 Transactions of the Royal Society of London Series A,
 909 370, 2765, doi: [10.1098/rsta.2011.0269](https://doi.org/10.1098/rsta.2011.0269)
 910 Apai, D., Rackham, B. V., Giampapa, M. S., et al. 2018,
 911 arXiv e-prints, arXiv:1803.08708,
 912 doi: [10.48550/arXiv.1803.08708](https://doi.org/10.48550/arXiv.1803.08708)
 913 Astropy Collaboration, Robitaille, T. P., Tollerud, E. J.,
 914 et al. 2013, A&A, 558, A33,
 915 doi: [10.1051/0004-6361/201322068](https://doi.org/10.1051/0004-6361/201322068)
 916 Astropy Collaboration, Price-Whelan, A. M., Sipőcz, B. M.,
 917 et al. 2018, AJ, 156, 123, doi: [10.3847/1538-3881/aabc4f](https://doi.org/10.3847/1538-3881/aabc4f)
 918 Barclay, T., Kostov, V. B., Colón, K. D., et al. 2021, AJ,
 919 162, 300, doi: [10.3847/1538-3881/ac2824](https://doi.org/10.3847/1538-3881/ac2824)
 920 Barclay, T., Sheppard, K. B., Latouf, N., et al. 2023, arXiv
 921 e-prints, arXiv:2301.10866,
 922 doi: [10.48550/arXiv.2301.10866](https://doi.org/10.48550/arXiv.2301.10866)
 923 Batalha, N., Freedman, R., Lupu, R., & Marley, M. 2020,
 924 Resampled Opacity Database for PICASO v2, 1.0,
 925 Zenodo, doi: [10.5281/zenodo.3759675](https://doi.org/10.5281/zenodo.3759675)
 926 Batalha, N. E., Lewis, T., Fortney, J. J., et al. 2019, ApJL,
 927 885, L25, doi: [10.3847/2041-8213/ab4909](https://doi.org/10.3847/2041-8213/ab4909)
 928 Bell, T. J., Ahrer, E.-M., Brande, J., et al. 2022, arXiv
 929 e-prints, arXiv:2207.03585,
 930 <https://arxiv.org/abs/2207.03585>
 931 Benneke, B., & Seager, S. 2013, ApJ, 778, 153,
 932 doi: [10.1088/0004-637X/778/2/153](https://doi.org/10.1088/0004-637X/778/2/153)
 933 Birkmann, S. M., Ferruit, P., Giardino, G., et al. 2022,
 934 A&A, 661, A83, doi: [10.1051/0004-6361/202142592](https://doi.org/10.1051/0004-6361/202142592)
 935 Bourque, M., Espinoza, N., Filippazzo, J., et al. 2021, The
 936 Exoplanet Characterization Toolkit (ExoCTK), 1.0.0,
 937 Zenodo, doi: [10.5281/zenodo.4556063](https://doi.org/10.5281/zenodo.4556063)

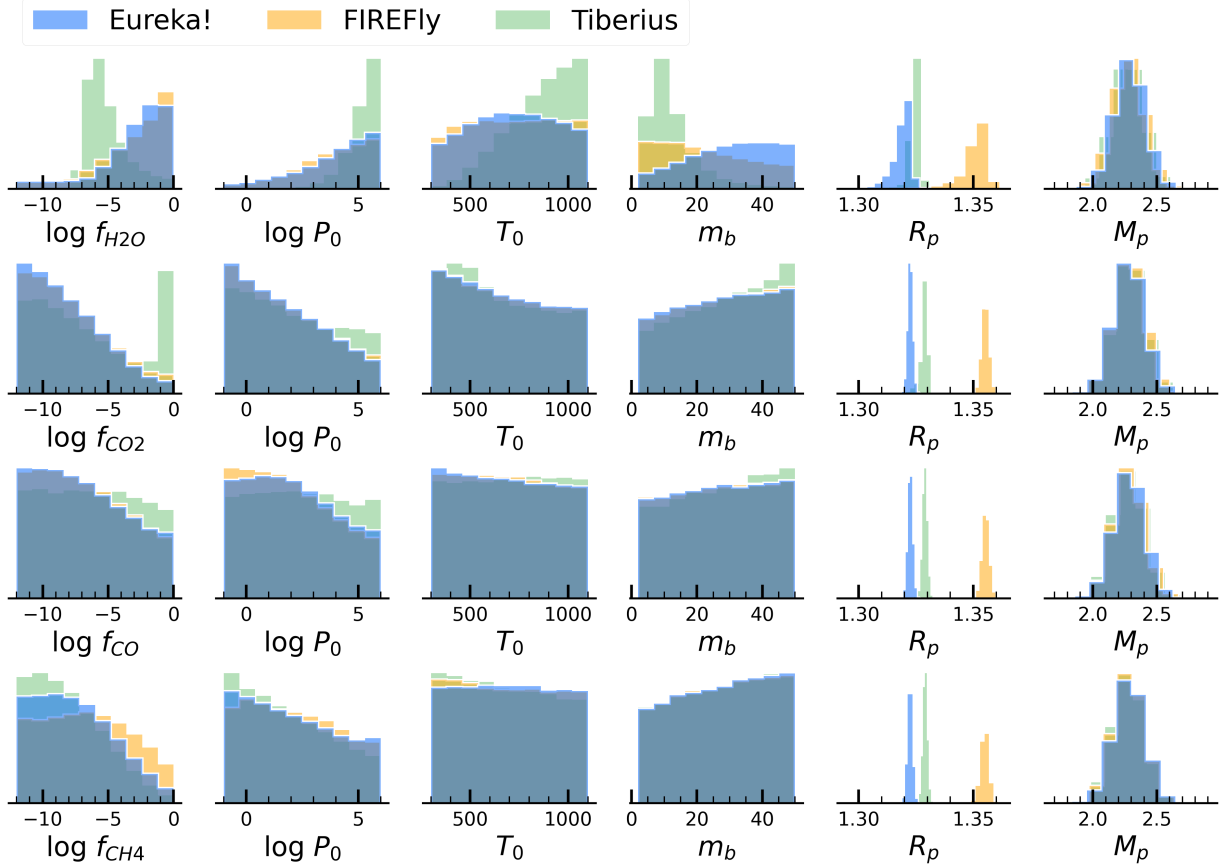


Figure 7. The 1D posteriors for *rfast* single-gas retrievals. From top to bottom water, carbon dioxide, carbon monoxide, and methane. Each reduction is shown in its own color with Eureka! in blue, FIREFLY in orange and Tiberius in green.

- 938 Buchner, J., Georgakakis, A., Nandra, K., et al. 2014,
 939 A&A, 564, A125, doi: [10.1051/0004-6361/201322971](https://doi.org/10.1051/0004-6361/201322971)
 940 Bushouse, H., Eisenhamer, J., Dencheva, N., et al. 2022,
 941 JWST Calibration Pipeline, 1.8.2, Zenodo,
 942 doi: [10.5281/zenodo.7325378](https://doi.org/10.5281/zenodo.7325378)
 943 Caballero, J. A., González-Álvarez, E., Brady, M., et al.
 944 2022, A&A, 665, A120,
 945 doi: [10.1051/0004-6361/202243548](https://doi.org/10.1051/0004-6361/202243548)
 946 Chen, J., & Kipping, D. 2017, ApJ, 834, 17,
 947 doi: [10.3847/1538-4357/834/1/17](https://doi.org/10.3847/1538-4357/834/1/17)
 948 Damiano, M., Hu, R., Barclay, T., et al. 2022, AJ, 164, 225,
 949 doi: [10.3847/1538-3881/ac9472](https://doi.org/10.3847/1538-3881/ac9472)
 950 de Wit, J., Wakeford, H. R., Gillon, M., et al. 2016, Nature,
 951 537, 69, doi: [10.1038/nature18641](https://doi.org/10.1038/nature18641)
 952 de Wit, J., Wakeford, H. R., Lewis, N. K., et al. 2018,
 953 Nature Astronomy, 2, 214,
 954 doi: [10.1038/s41550-017-0374-z](https://doi.org/10.1038/s41550-017-0374-z)
 955 Diamond-Lowe, H., Berta-Thompson, Z., Charbonneau, D.,
 956 & Kempton, E. M. R. 2018, AJ, 156, 42,
 957 doi: [10.3847/1538-3881/aac6dd](https://doi.org/10.3847/1538-3881/aac6dd)
 958 Diamond-Lowe, H., Charbonneau, D., Malik, M., Kempton,
 959 E. M. R., & Beletsky, Y. 2020, AJ, 160, 188,
 960 doi: [10.3847/1538-3881/abaf4f](https://doi.org/10.3847/1538-3881/abaf4f)
 961 Diamond-Lowe, H., Mendonça, J. M., Charbonneau, D., &
 962 Buchhave, L. A. 2022, arXiv e-prints, arXiv:2210.11809,
 963 doi: [10.48550/arXiv.2210.11809](https://doi.org/10.48550/arXiv.2210.11809)
 964 Feroz, F., Hobson, M. P., & Bridges, M. 2009, MNRAS,
 965 398, 1601, doi: [10.1111/j.1365-2966.2009.14548.x](https://doi.org/10.1111/j.1365-2966.2009.14548.x)
 966 Foreman-Mackey, D., Hogg, D. W., Lang, D., & Goodman,
 967 J. 2013, PASP, 125, 306, doi: [10.1086/670067](https://doi.org/10.1086/670067)
 968 Gaia Collaboration, Brown, A. G. A., Vallenari, A., et al.
 969 2021, A&A, 649, A1, doi: [10.1051/0004-6361/202039657](https://doi.org/10.1051/0004-6361/202039657)
 970 Gao, P., Thorngren, D. P., Lee, E. K. H., et al. 2020, Nature
 971 Astronomy, 4, 951, doi: [10.1038/s41550-020-1114-3](https://doi.org/10.1038/s41550-020-1114-3)
 972 Garcia, L. J., Moran, S. E., Rackham, B. V., et al. 2022,
 973 A&A, 665, A19, doi: [10.1051/0004-6361/202142603](https://doi.org/10.1051/0004-6361/202142603)
 974 Goldblatt, C., Robinson, T. D., Zahnle, K. J., & Crisp, D.
 975 2013, Nature Geoscience, 6, 661, doi: [10.1038/ngeo1892](https://doi.org/10.1038/ngeo1892)
 976 Grant, D., & Wakeford, H. R. 2022, Exo-TiC/ExoTiC-LD:
 977 ExoTiC-LD v3.0.0, v3.0.0, Zenodo,
 978 doi: [10.5281/zenodo.7437681](https://doi.org/10.5281/zenodo.7437681)

- Gressier, A., Mori, M., Changeat, Q., et al. 2022, *A&A*, 658, A133, doi: [10.1051/0004-6361/202142140](https://doi.org/10.1051/0004-6361/202142140)
- Harris, C. R., Millman, K. J., van der Walt, S. J., et al. 2020, *Nature*, 585, 357, doi: [10.1038/s41586-020-2649-2](https://doi.org/10.1038/s41586-020-2649-2)
- Horne, K. 1986, *Publ. Astron. Soc. Pac.*, 98, 609, doi: [10.1086/131801](https://doi.org/10.1086/131801)
- Hunter, J. D. 2007, *Computing in Science Engineering*, 9, 90, doi: [10.1109/MCSE.2007.55](https://doi.org/10.1109/MCSE.2007.55)
- Jakobsen, P., Ferruit, P., Alves de Oliveira, C., et al. 2022, *A&A*, 661, A80, doi: [10.1051/0004-6361/202142663](https://doi.org/10.1051/0004-6361/202142663)
- Kaltenegger, L., & Traub, W. A. 2009, *ApJ*, 698, 519, doi: [10.1088/0004-637X/698/1/519](https://doi.org/10.1088/0004-637X/698/1/519)
- Karman, T., Gordon, I. E., van der Avoird, A., et al. 2019, *Icarus*, 328, 160, doi: [10.1016/j.icarus.2019.02.034](https://doi.org/10.1016/j.icarus.2019.02.034)
- Kasting, J. F., & Pollack, J. B. 1983, *Icarus*, 53, 479, doi: [10.1016/0019-1035\(83\)90212-9](https://doi.org/10.1016/0019-1035(83)90212-9)
- Kempton, E. M. R., Bean, J. L., Louie, D. R., et al. 2018, *PASP*, 130, 114401, doi: [10.1088/1538-3873/aad6f6](https://doi.org/10.1088/1538-3873/aad6f6)
- Kirk, J., López-Morales, M., Wheatley, P. J., et al. 2019, *AJ*, 158, 144, doi: [10.3847/1538-3881/ab397d](https://doi.org/10.3847/1538-3881/ab397d)
- Kirk, J., Wheatley, P. J., Loudon, T., et al. 2018, *MNRAS*, 474, 876, doi: [10.1093/mnras/stx2826](https://doi.org/10.1093/mnras/stx2826)
- Kirk, J., Rackham, B. V., MacDonald, R. J., et al. 2021, *AJ*, 162, 34, doi: [10.3847/1538-3881/abfcd2](https://doi.org/10.3847/1538-3881/abfcd2)
- Kostogryz, N., Shapiro, A. I., Witzke, V., et al. 2023, *Research Notes of the American Astronomical Society*, 7, 39, doi: [10.3847/2515-5172/acc180](https://doi.org/10.3847/2515-5172/acc180)
- Kreidberg, L. 2015, *PASP*, 127, 1161, doi: [10.1086/683602](https://doi.org/10.1086/683602)
- Kreidberg, L., Line, M. R., Bean, J. L., et al. 2015, *ApJ*, 814, 66, doi: [10.1088/0004-637X/814/1/66](https://doi.org/10.1088/0004-637X/814/1/66)
- Kreidberg, L., Koll, D. D. B., Morley, C., et al. 2019, *Nature*, 573, 87, doi: [10.1038/s41586-019-1497-4](https://doi.org/10.1038/s41586-019-1497-4)
- Li, G., Gordon, I. E., Rothman, L. S., et al. 2015, *The Astrophysical Journal Supplement Series*, 216, 15, doi: [10.1088/0067-0049/216/1/15](https://doi.org/10.1088/0067-0049/216/1/15)
- Libby-Roberts, J. E., Berta-Thompson, Z. K., Diamond-Lowe, H., et al. 2022, *AJ*, 164, 59, doi: [10.3847/1538-3881/ac75de](https://doi.org/10.3847/1538-3881/ac75de)
- Lincowski, A. P., Meadows, V. S., Crisp, D., et al. 2018, *ApJ*, 867, 76, doi: [10.3847/1538-4357/aae36a](https://doi.org/10.3847/1538-4357/aae36a)
- Line, M. R., Knutson, H., Wolf, A. S., & Yung, Y. L. 2014, *ApJ*, 783, 70, doi: [10.1088/0004-637X/783/2/70](https://doi.org/10.1088/0004-637X/783/2/70)
- Line, M. R., & Yung, Y. L. 2013, *ApJ*, 779, 3, doi: [10.1088/0004-637X/779/1/3](https://doi.org/10.1088/0004-637X/779/1/3)
- Loyd, R. O. P., Shkolnik, E. L., Schneider, A. C., et al. 2021, *ApJ*, 907, 91, doi: [10.3847/1538-4357/abd0f0](https://doi.org/10.3847/1538-4357/abd0f0)
- Lustig-Yaeger, J., Meadows, V. S., & Lincowski, A. P. 2019, *ApJL*, 887, L11, doi: [10.3847/2041-8213/ab5965](https://doi.org/10.3847/2041-8213/ab5965)
- Lustig-Yaeger, J., Fu, G., May, E. M., et al. 2023, *arXiv e-prints*, arXiv:2301.04191, doi: [10.48550/arXiv.2301.04191](https://doi.org/10.48550/arXiv.2301.04191)
- MacDonald, R. J. 2023, *The Journal of Open Source Software*, 8, 4873, doi: [10.21105/joss.04873](https://doi.org/10.21105/joss.04873)
- MacDonald, R. J., & Madhusudhan, N. 2017, *MNRAS*, 469, 1979, doi: [10.1093/mnras/stx804](https://doi.org/10.1093/mnras/stx804)
- Magic, Z., Chiavassa, A., Collet, R., & Asplund, M. 2015, *Astronomy & Astrophysics*, 573, A90
- Mansfield, M., Bean, J. L., Kempton, E. M. R., et al. 2021, *Constraining the Atmosphere of the Terrestrial Exoplanet Gl486b*, *JWST Proposal. Cycle 1*, ID. #1743
- Mansfield, M., Kite, E. S., Hu, R., et al. 2019, *ApJ*, 886, 141, doi: [10.3847/1538-4357/ab4c90](https://doi.org/10.3847/1538-4357/ab4c90)
- McIntyre, S. R. N., King, P. L., & Mills, F. P. 2023, *MNRAS*, 519, 6210, doi: [10.1093/mnras/stad095](https://doi.org/10.1093/mnras/stad095)
- Moran, S. E., Hörst, S. M., Batalha, N. E., Lewis, N. K., & Wakeford, H. R. 2018, *AJ*, 156, 252, doi: [10.3847/1538-3881/aae83a](https://doi.org/10.3847/1538-3881/aae83a)
- Mugnai, L. V., Modirrousta-Galian, D., Edwards, B., et al. 2021, *AJ*, 161, 284, doi: [10.3847/1538-3881/abf3c3](https://doi.org/10.3847/1538-3881/abf3c3)
- Peacock, S., Barman, T., Shkolnik, E. L., Hauschildt, P. H., & Baron, E. 2019, *ApJ*, 871, 235, doi: [10.3847/1538-4357/aaf891](https://doi.org/10.3847/1538-4357/aaf891)
- Pérez, F., & Granger, B. E. 2007, *Computing in Science and Engineering*, 9, 21, doi: [10.1109/MCSE.2007.53](https://doi.org/10.1109/MCSE.2007.53)
- Pidhorodetska, D., Moran, S. E., Schwieterman, E. W., et al. 2021, *AJ*, 162, 169, doi: [10.3847/1538-3881/ac1171](https://doi.org/10.3847/1538-3881/ac1171)
- Pinhas, A., Rackham, B. V., Madhusudhan, N., & Apai, D. 2018, *MNRAS*, 480, 5314, doi: [10.1093/mnras/sty2209](https://doi.org/10.1093/mnras/sty2209)
- Polyansky, O. L., Kyuberis, A. A., Zobov, N. F., et al. 2018, *MNRAS*, 480, 2597, doi: [10.1093/mnras/sty1877](https://doi.org/10.1093/mnras/sty1877)
- Powell, M. J. D. 1964, *The Computer Journal*, 7, 155, doi: [10.1093/comjnl/7.2.155](https://doi.org/10.1093/comjnl/7.2.155)
- Rackham, B. V., Apai, D., & Giampapa, M. S. 2018, *ApJ*, 853, 122, doi: [10.3847/1538-4357/aaa08c](https://doi.org/10.3847/1538-4357/aaa08c)
- Rackham, B. V., Espinoza, N., Berdyugina, S. V., et al. 2022, *arXiv e-prints*, arXiv:2201.09905, doi: [10.48550/arXiv.2201.09905](https://doi.org/10.48550/arXiv.2201.09905)
- Rathcke, A. D., MacDonald, R. J., Barstow, J. K., et al. 2021, *AJ*, 162, 138, doi: [10.3847/1538-3881/ac0e99](https://doi.org/10.3847/1538-3881/ac0e99)
- Ridden-Harper, A., Nugroho, S., Flagg, L., et al. 2022, *arXiv e-prints*, arXiv:2212.11816, doi: [10.48550/arXiv.2212.11816](https://doi.org/10.48550/arXiv.2212.11816)
- Rigby, J., Perrin, M., McElwain, M., et al. 2022, *arXiv e-prints*, arXiv:2207.05632, <https://arxiv.org/abs/2207.05632>
- Robinson, T. D., & Salvador, A. 2023, *PSJ*, 4, 10, doi: [10.3847/PSJ/acac9a](https://doi.org/10.3847/PSJ/acac9a)

- 1076 Rogers, J. G., Gupta, A., Owen, J. E., & Schlichting, H. E.
 1077 2021, MNRAS, 508, 5886, doi: [10.1093/mnras/stab2897](https://doi.org/10.1093/mnras/stab2897)
- 1078 Rogers, L. A. 2015, ApJ, 801, 41,
 1079 doi: [10.1088/0004-637X/801/1/41](https://doi.org/10.1088/0004-637X/801/1/41)
- 1080 Rustamkulov, Z., Sing, D. K., Liu, R., & Wang, A. 2022,
 1081 ApJL, 928, L7, doi: [10.3847/2041-8213/ac5b6f](https://doi.org/10.3847/2041-8213/ac5b6f)
- 1082 Rustamkulov, Z., Sing, D. K., Mukherjee, S., et al. 2023,
 1083 Nature, 614, 659, doi: [10.1038/s41586-022-05677-y](https://doi.org/10.1038/s41586-022-05677-y)
- 1084 Salvatier, J., Wiecki, T. V., & Fonnesbeck, C. 2016,
 1085 PyMC3: Python probabilistic programming framework,
 1086 Astrophysics Source Code Library, record ascl:1610.016.
 1087 <http://ascl.net/1610.016>
- 1088 Sandford, E., & Kipping, D. 2017, AJ, 154, 228,
 1089 doi: [10.3847/1538-3881/aa94bf](https://doi.org/10.3847/1538-3881/aa94bf)
- 1090 Seager, S., & Mallén-Ornelas, G. 2003, ApJ, 585, 1038,
 1091 doi: [10.1086/346105](https://doi.org/10.1086/346105)
- 1092 Somers, G., Cao, L., & Pinsonneault, M. H. 2020, ApJ, 891,
 1093 29, doi: [10.3847/1538-4357/ab722e](https://doi.org/10.3847/1538-4357/ab722e)
- 1094 Sossi, P. A., Tollan, P. M. E., Badro, J., & Bower, D. J.
 1095 2023, Earth and Planetary Science Letters, 601, 117894,
 1096 doi: [10.1016/j.epsl.2022.117894](https://doi.org/10.1016/j.epsl.2022.117894)
- 1097 Speagle, J. S. 2020, MNRAS, 493, 3132,
 1098 doi: [10.1093/mnras/staa278](https://doi.org/10.1093/mnras/staa278)
- 1099 STScI Development Team. 2013, pysynphot: Synthetic
 1100 photometry software package, Astrophysics Source Code
 1101 Library, record ascl:1303.023. <http://ascl.net/1303.023>
- 1102 Tashkun, S. A., & Perevalov, V. I. 2011, Journal of
 1103 Quantitative Spectroscopy and Radiative Transfer, 112,
 1104 1403, doi: [10.1016/j.jqsrt.2011.03.005](https://doi.org/10.1016/j.jqsrt.2011.03.005)
- 1105 The JWST Transiting Exoplanet Community Early Release
 1106 Science Team, Ahrer, E.-M., Alderson, L., et al. 2022,
 1107 arXiv e-prints, arXiv:2208.11692.
 1108 <https://arxiv.org/abs/2208.11692>
- 1109 Tian, M., & Heng, K. 2023, arXiv e-prints,
 1110 arXiv:2301.10217, doi: [10.48550/arXiv.2301.10217](https://doi.org/10.48550/arXiv.2301.10217)
- 1111 Trifonov, T., Caballero, J. A., Morales, J. C., et al. 2021,
 1112 Science, 371, 1038, doi: [10.1126/science.abd7645](https://doi.org/10.1126/science.abd7645)
- 1113 Trotta, R. 2008, Contemporary Physics, 49, 71,
 1114 doi: [10.1080/00107510802066753](https://doi.org/10.1080/00107510802066753)
- 1115 —. 2017, arXiv e-prints, arXiv:1701.01467,
 1116 doi: [10.48550/arXiv.1701.01467](https://doi.org/10.48550/arXiv.1701.01467)
- 1117 van der Walt, S., Colbert, S. C., & Varoquaux, G. 2011,
 1118 Computing in Science Engineering, 13, 22,
 1119 doi: [10.1109/MCSE.2011.37](https://doi.org/10.1109/MCSE.2011.37)
- 1120 Virtanen, P., Gommers, R., Oliphant, T. E., et al. 2020,
 1121 Nature Methods, 17, 261,
 1122 doi: <https://doi.org/10.1038/s41592-019-0686-2>
- 1123 Wakeford, H. R., Lewis, N. K., Fowler, J., et al. 2019, AJ,
 1124 157, 11, doi: [10.3847/1538-3881/aaf04d](https://doi.org/10.3847/1538-3881/aaf04d)
- 1125 Wordsworth, R., & Kreidberg, L. 2022, ARA&A, 60, 159,
 1126 doi: [10.1146/annurev-astro-052920-125632](https://doi.org/10.1146/annurev-astro-052920-125632)
- 1127 Yurchenko, S. N., Amundsen, D. S., Tennyson, J., &
 1128 Waldmann, I. P. 2017, Astronomy and Astrophysics, 605,
 1129 A95, doi: [10.1051/0004-6361/201731026](https://doi.org/10.1051/0004-6361/201731026)
- 1130 Zahnle, K. J., & Catling, D. C. 2017, The Astrophysical
 1131 Journal, 843, 122, doi: [10.3847/1538-4357/aa7846](https://doi.org/10.3847/1538-4357/aa7846)
- 1132 Zahnle, K. J., Kasting, J. F., & Pollack, J. B. 1988, Icarus,
 1133 74, 62, doi: [10.1016/0019-1035\(88\)90031-0](https://doi.org/10.1016/0019-1035(88)90031-0)
- 1134 Zhang, Z., Zhou, Y., Rackham, B. V., & Apai, D. 2018, AJ,
 1135 156, 178, doi: [10.3847/1538-3881/aade4f](https://doi.org/10.3847/1538-3881/aade4f)
- 1136 Zhou, L., Ma, B., Wang, Y.-H., & Zhu, Y.-N. 2023,
 1137 Research in Astronomy and Astrophysics, 23, 025011,
 1138 doi: [10.1088/1674-4527/acaceb](https://doi.org/10.1088/1674-4527/acaceb)